

HIGH REDSHIFT X-RAY COOLING-CORE CLUSTER ASSOCIATED WITH THE LUMINOUS RADIO LOUD QUASAR 3C186

ANETA SIEMIGINOWSKA¹, D.J. BURKE¹, THOMAS L. ALDCROFT¹, D.M. WORRALL², S.ALLEN³,
JILL BECHTOLD⁴, TRACY CLARKE⁵, C.C.CHEUNG⁶

¹ Harvard Smithsonian Center for Astrophysics, 60 Garden St, Cambridge, MA 02138

² H.H. Wills Physics Laboratory, University of Bristol, Tyndall Avenue, Bristol BS8 1TL, UK

³ Kavli Institute for Particle Astrophysics and Cosmology, Stanford University, 382 Via Pueblo Mall, Stanford, CA 94305-4060, USA

⁴ Steward Observatory, University of Arizona, Tucson, AZ

⁵ Naval Research Laboratory, Code 7200, 4555 Overlook Ave SW, Washington, DC 20375

⁶ National Research Council Research Associate, Space Science Division, Naval Research Laboratory, Washington, DC 20375, USA
asiemiginowska@cfa.harvard.edu

October 30, 2018

ABSTRACT

We present the first results from a new, deep (200ks) *Chandra* observation of the X-ray luminous galaxy cluster surrounding the powerful ($L \sim 10^{47}$ erg s⁻¹), high-redshift ($z = 1.067$), compact-steep-spectrum radio-loud quasar 3C 186. The diffuse X-ray emission from the cluster has a roughly ellipsoidal shape and extends out to radii of at least ~ 60 arcsec (~ 500 kpc). The centroid of the diffuse X-ray emission is offset by $0.68 \pm 0.11''$ ($\sim 5.5 \pm 0.9$ kpc) from the position of the quasar. We measure a cluster mass within the radius at which the mean enclosed density is 2500 times the critical density, $r_{2500} = 283_{-13}^{+18}$ kpc, of $1.02_{-0.14}^{+0.21} \times 10^{14} M_{\odot}$. The gas mass fraction within this radius is $f_{gas} = 0.129_{-0.016}^{+0.015}$. This value is consistent with measurements at lower redshifts and implies minimal evolution in the $f_{gas}(z)$ relation for hot, massive clusters at $0 < z < 1.1$. The measured metal abundance of $0.42_{-0.07}^{+0.08}$ Solar is consistent with the abundance observed in other massive, high redshift clusters. The spatially-resolved temperature profile for the cluster shows a drop in temperature, from $kT \sim 8$ keV to $kT \sim 3$ keV, in its central regions that is characteristic of cooling core clusters. This is the first spectroscopic identification of a cooling core cluster at $z > 1$. We measure cooling times for the X-ray emitting gas at radii of 50 kpc and 25 kpc of $1.7 \pm 0.2 \times 10^9$ years and $7.5 \pm 2.6 \times 10^8$ years, as well as a nominal cooling rate (in the absence of heating) of $400 \pm 190 M_{\odot} \text{year}^{-1}$ within the central 100 kpc. In principle, the cooling gas can supply enough fuel to support the growth of the supermassive black hole and to power the luminous quasar. The radiative power of the quasar exceeds by a factor of 10 the kinematic power of the central radio source, suggesting that radiative heating may be important at intermittent intervals in cluster cores.

Subject headings: quasars: individual (3C 186) - X-rays: galaxies: clusters

1. INTRODUCTION

Recent X-ray observations of nearby galaxy clusters show that powerful outbursts of their central cD galaxies have imprinted a rich variety of structures onto the X-ray emitting gas (see McNamara & Nulsen (2007) for a review). The amount of energy supplied into the cluster gas by these outbursts can prevent the clusters from cooling (McNamara et al. 2005). The average power released in outbursts exceeds $\sim 10^{45}$ erg s⁻¹. This is equivalent to the typical radiative power of a quasar. However, the central cD galaxy is usually observed in a quiescent, non-luminous, state. The impact of a luminous quasar on the cluster gas has not been widely explored so far.

On the other hand, it has been known for a long time that powerful radio-loud quasars are associated with rich galaxy environments (Smith & Heckman 1990; Ellingson et al. 1991a; Yee & Ellingson 1993), and so we should be able to find luminous radio loud quasars in X-ray-bright clusters. Much remains unknown about the details of how quasar activity is triggered, the way in which the accretion proceeds, the impact of the quasar on its galactic and cluster environment, and which physical pro-

cesses are important as a function of redshift. X-ray clusters retain the history of the cD activity and studies of quasars in X-ray clusters can provide some answers to these questions.

There have been a few successful searches for the diffuse X-ray cluster emission surrounding powerful quasars and radio galaxies using ROSAT (Crawford & Fabian 1993; Worrall et al. 1994; Hall et al. 1995, 1997; Crawford et al. 1999; Hardcastle & Worrall 1999; Sarazin et al. 1999; Worrall et al. 2000). Hall et al. (1997) discussed the ROSAT X-ray data for five quasars located in X-ray clusters, and concluded that simple models for triggering the quasars (e.g., cooling flows, a low-pressure ISM, or low velocity dispersions) do not work, suggesting instead that mergers and strong interactions are critical in delivering the gas to the quasar host. Hardcastle & Worrall (1999) analyzed a large sample of powerful radio sources and found cases of extended X-ray emission that are likely to be of cluster origin. However, the number of such cases was limited to eight by ROSAT's sensitivity and some of these were not confirmed by *Chandra* observations (Crawford & Fabian 2003; Worrall et al. 2004). Extended

X-ray emission can be associated alternatively with radio structures such as large scale jets, knots, hot spots, and lobes (e.g., Celotti & Fabian 2004; Kataoka & Stawarz 2005; Croston et al. 2005; Harris & Krawczynski 2006) and disentangling the cluster emission from the other X-ray emission components has been challenging. The *Chandra* X-ray Observatory (Weisskopf et al. 2000) has both the spatial resolution and the dynamic range necessary to study diffuse X-ray emission in the vicinity of a strong point source, and allows the separation of cluster X-ray emission from that of jets and other structures.

Belsole et al. (2007) studied a *Chandra* and XMM-*Newton* sample of twenty powerful radio sources at $z > 0.5$, including two core-dominated quasars, and found diffuse X-ray emission in 60% of the sample. The diffuse emission was faint, but the luminosities were consistent with non-quasar-host X-ray clusters at similar and lower redshifts, and the work found no difference between the cluster environments of quasars and radio galaxies.

We discovered a bright X-ray cluster in a pointed *Chandra* observation of the radio-loud compact steep spectrum (CSS) quasar 3C186 at the redshift of $z = 1.067$ (Siemiginowska et al. 2005). This observation, although only ~ 30 ksec long, provided an X-ray luminosity measurement, $L_{(0.5-2\text{keV})} = 6 \times 10^{44}$ erg s^{-1} , a cluster temperature ($kT = 5.2_{-0.9}^{+1.3}$ keV) and a gas-mass fraction ($f_{\text{gas}}(r_{2500}) \sim 0.13 \pm 0.08$) that were typical of other massive, relaxed clusters (Vikhlinin et al. 2002; Allen et al. 2008). The 3C186 X-ray cluster is more luminous than the Belsole et al. (2007) clusters, and provides a unique opportunity to study a luminous cluster associated with a quasar at high redshift. The powerful and luminous quasar, $L_{\text{bol}} \sim 10^{47}$ erg s^{-1} , is located well within the diffuse X-ray emission.

Here we report the results from a 200 ks deep follow-up *Chandra* observation of 3C186, made in order to study the quasar and its associated cluster in greater detail. Relatively few massive, relaxed X-ray clusters at $z > 1$ are known. In addition, the 3C186 cluster is one of very few X-ray clusters that is both associated with a quasar and bright enough for detailed study. We give details of the *Chandra* observation in Section 2, describe image and spectral analyzes in Section 3, and present a discussion of the results in Section 4.

Throughout this paper we use cosmological parameters based on WMAP measurements (Spergel et al. 2003): $H_0 = 71$ km s^{-1} Mpc $^{-1}$, $\Omega_M = 0.27$, and $\Omega_{\text{vac}} = 0.73$. At $z = 1.067$, $1''$ corresponds to ~ 8.163 kpc.

2. CHANDRA OBSERVATIONS

3C186 was observed with the *Chandra* ACIS-S CCD in December 2007. Due to scheduling constraints the observation was split into four separate pointings that sum to a total exposure of 197 ks (see Table 1). The quasar was placed on the back-illuminated CCD (S3) and was offset by -1 arcmin in Y coordinates to make sure that the cluster is not affected by a chip gap. The observation was made in VFAINT mode and full-window mode. Table 1 shows which CCD chips were active. The observation was not affected by solar flares, and the background was quiet

for the entire observation. The quasar is slightly offset in obsid 9408 with respect to the other three observations in Z coordinates. However, the four observations were performed with similar enough configurations that they could be merged together for the purpose of image analysis. Note that the exposure maps are flat on the scale size of the cluster in all four observations. Analysis was performed with the CIAO version 4 software using CALDB version 4.2. All modeling was done in *Sherpa* (Freeman et al. 2001; Refsdal et al. 2009). We used the Cash and Cstat fitting statistics (Cash 1979) and the Nelder-Mead optimization method (Nelder & Mead 1965). We did not subtract the background, but included a background contribution in the model expressions for all of our model fitting.

The events have been filtered to remove the VFAINT background events. The standard ± 0.5 pixel randomization has also been removed before merging the four observations. The ACIS image of the merged observation is shown in Figure 3.1. The bright quasar is located within diffuse X-ray emission that is visible on a scale exceeding $\sim 30''$ (250 kpc).

3. DATA ANALYSIS AND RESULTS

3.1. Image Analysis

We performed 2D image analysis using the merged data to evaluate the spatial extent of the diffuse emission, and the quasar contribution to the diffuse emission within < 5 arcsec of the core. Figure 3.1 shows the merged ACIS-S images in three RGB colors representing different energy ranges: red corresponds to 0.3-1.5 keV, green to 1.5-2.5 keV, and blue to 2.5-7 keV. We show a binned image with the standard ACIS-S pixel size of $0.492''$ and an image that is smoothed with a Gaussian kernel ($\sigma = 2.46''$). The cluster emission is relatively smooth, elliptical, and elongated in NE-SW direction. We measure (using ds9) the largest extent of the emission to be $\sim 128''$ along the major axis at PA = 43 deg, i.e. $\sim 60''$ (> 500 kpc) distance from the quasar. We selected the events within a 0.5-7 keV energy range for the spatial modeling.

Effects of the strong quasar emission have been taken into account in the analysis of the cluster data. Note that point sources in the field of view in Figure 3.1 indicate the size of the PSF for a source of typical strength. We adopted the observed quasar spectrum (a power law with a photon index of $\Gamma = 1.9$) as the input model for CHART¹ simulations of the quasar's PSF, and created a very high signal-to-noise PSF model image for use in our analysis.

In our two-dimensional analysis we fitted both the cluster centroid and the quasar position to determine whether they are co-aligned. We tried circular models and also allowed the cluster gas to have an ellipticity. We used *Sherpa* and adopted a 2D Gaussian² model for the quasar and a 2D Beta model for the cluster. We also included a constant model to account for the background. Because the exposure map is uniform across the cluster region we did not include the exposure map in this analysis, and so we worked with the count data and used Poisson statistics in fitting. However, we have confirmed that including the exposure map gives consistent parameters with the ones reported here.

¹ <http://cxc.harvard.edu/chart/index.html>

² We used Gaussian model instead of a Delta function to account for an unknown aspect "blur" in MARX.

TABLE 1
Chandra OBSERVATIONS

OBSID	Exposure (ks)	Date	CCD	Inner ^a 2.5-6.0"	Outer ^a 6-20"
9407	66.3	2007-12-03	ACIS-23567	500.0±22.8	1000.7±34.8
9774	75.1	2007-12-06	ACIS-23567	613.0±25.3	1110.6±36.9
9775	15.9	2007-12-08	ACIS-23567	114.8±11.0	241.5±17.4
9408	39.6	2007-12-11	ACIS-23567	306.9±17.8	627.9±27.3

^a net counts within the energy range 0.3-7 keV in annuli centered on the quasar whose radii are given in arcsec.

We used *Sherpa* to convolve the 2D model with the simulated 2D PSF, and fitted the result to the data. The models and best-fit parameters are given in Table 2.

The 2D fit finds a cluster core radius of $r_{core} = 3.51 \pm 0.31$ arcsec ($\sim 28.6 \pm 2.5$ kpc) and $\beta = 0.48 \pm 0.17$ for elliptical models and $r_{core} = 3.06 \pm 0.25$ arcsec ($\sim 25.0 \pm 2.0$ kpc) and $\beta = 0.48 \pm 0.17$ for the circular models. We note that there are systematic uncertainties present in the 2D analysis. The circular and elliptical fits have small statistical errors, but the difference between the parameters obtained in circular and elliptical models, in particular the cluster core radius, could be larger than the 1σ statistical errors reported in Table 2.

The best-fit locations of the quasar and the cluster centroids are offset by 0.68 arcsec, which is significantly greater than the corresponding uncertainty of 0.11 arcsec. We centered the surface brightness profile on the peak of the X-ray emission, while the true cluster centroid is slightly offset from the peak. Figure 2 shows surface-brightness profiles centered on the quasar and obtained from the data and the 2D best-fit circular models. The quasar emission dominates over the cluster emission within about 1.5 arcsec of the core and it is unresolved. At 2.5" distance from the peak the quasar contributes only about 10% of the total counts. The X-ray cluster emission dominates outside that region and exceeds the background level up to $\sim 40''$ (~ 320 kpc) from the quasar core. The cluster is detected at 3σ to ~ 285 kpc.

3.2. Spectral Modeling of the Cluster Emission

Based on our 2D image modeling results we assume that the X-ray emission outside the central 2.75" (~ 22 kpc) radius circular region is dominated by cluster emission (see analysis of the quasar contribution to the observed emission below). Note that 3C 186 is a compact radio source with a linear size of 2", so any X-ray emission associated with the radio source would be contained within this central region. We performed spectral analysis using each individual observation (obsid) and the corresponding calibration files. To obtain a global temperature for the entire cluster we extracted the spectrum from each event file (4 obsids) assuming a large elliptical region with the semi-minor and semi-major axis of 20" and 30" at PA 315 degree and ignoring the inner circle with radius of 2.75 arcsec dominated by the quasar. The background files were extracted from regions on the

same CCD located outside the source region excluding all the detected point sources. The APEC thermal plasma model at redshift $z = 1.067$ was fitted to the four spectra simultaneously, giving a best global temperature of $kT = 5.58^{+0.28}_{-0.27}$ keV, a metallicity of $0.42^{+0.08}_{-0.07}$ Solar and a soft-band flux $F_{0.5-2} = 8.27 \times 10^{-14}$ erg sec⁻¹ cm⁻² (Fig. 3). The best fit global cluster temperature is in agreement with the single temperature measured in the first short observation (Siemiginowska et al. 2005).

In order to look for any temperature gradient we extracted the spectra from each event file (4 obsid) assuming seven circular annuli centered on the quasar. The annuli cover the range from 2.75" to 30". We list the angular ranges spanned by the annuli in Table 3. All spectra were taken from individual observations to properly account for the instrumental effects. They were simultaneously fitted using all available counts for each annuli in the energy range 0.5-7 keV. We accounted for any background contribution using a complex empirical model (a combination of an 8th order polynomial and five Gaussian lines) that was first fitted to the ACIS-S "blank-sky" background data (see Appendix A1 for more details). We next fit this background model to the background spectra from each observation to check how well the model describes our data. In the simultaneous fit of the source and background model to the cluster spectra we varied only the background model normalization and kept all the other background model parameters frozen. We note that this is reasonable, as the fraction of background counts is typically lower than a few percent and exceeds 23% only in the outermost annulus.

Table 3 shows the best fit parameters for the applied model. We assumed an APEC model, included a correction for the Galactic absorption with an equivalent Hydrogen column density of $N_H = 5.64 \times 10^{20}$ cm⁻², and assumed cluster metal abundances of 0.3 in respect to Solar. We developed a *deproject* model³ in *Sherpa* based on the description in Fabian et al. (1981) and Kriss et al. (1983). We assume a spherical geometry and the radial sizes of the shells given by each individual annulus. The fit starts at the outermost annulus and proceeds towards the innermost one taking into account the contributions from outer annuli to the fitting of the inner one. The best-fit model gives the deprojected temperatures, normalizations, and densities listed in Table 3. We plot deprojected temperature, density and entropy profiles in Figure 4. These profiles are consistent with the cluster having a cooling core.

³ <http://cxc.harvard.edu/contrib/deproject/>

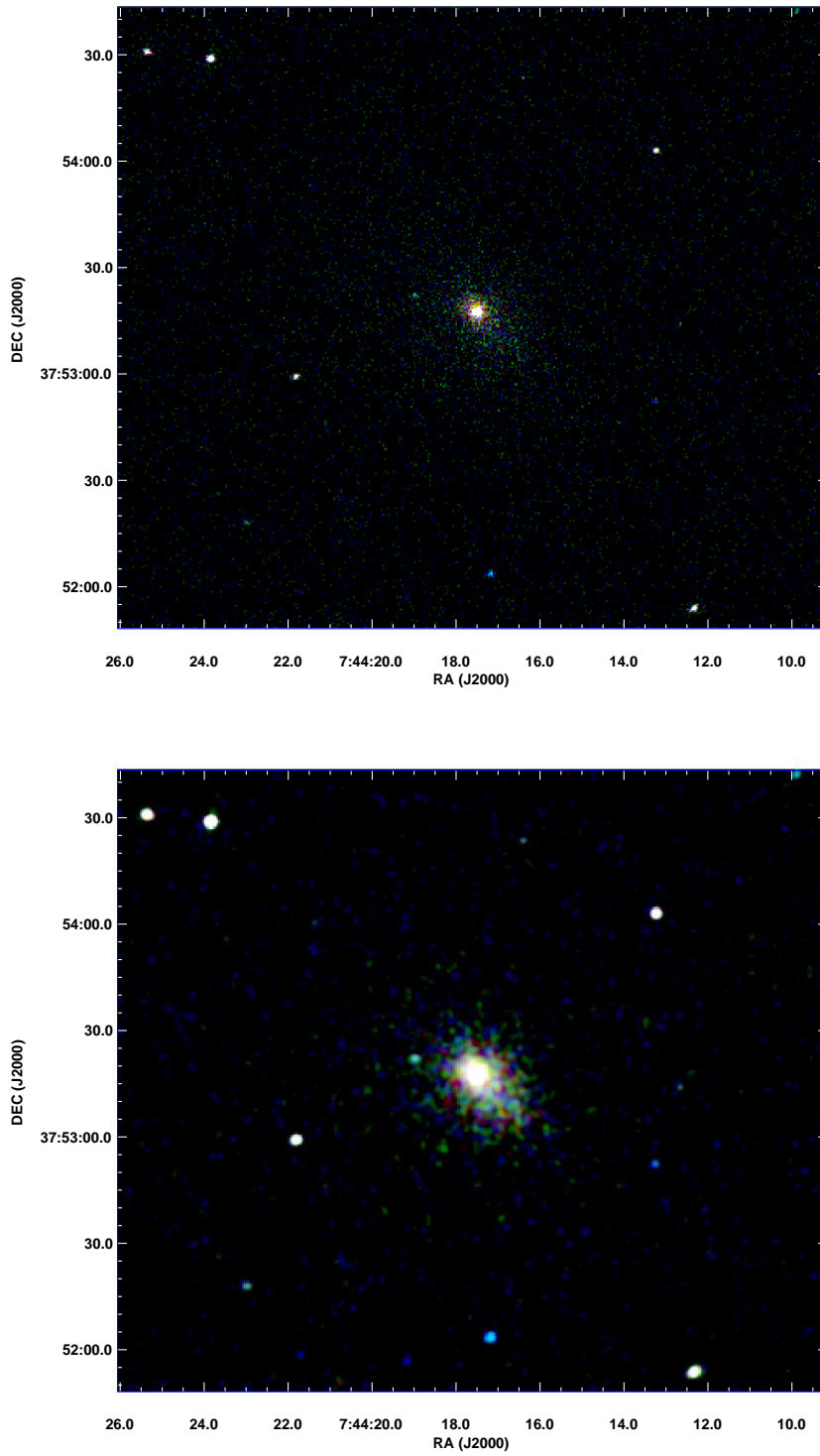


FIG. 1.— RGB color *Chandra* ACIS-S images of the 3C 186 X-ray cluster. The four individual observations have been merged into one image. Colors represent different energies: red:0.3-1.5 keV, green:1.5-2.5 keV and blue:2.5-7 keV. **Top:** Images binned to ACIS-S pixels with the standard size of 1 pixel=0.492 arcsec. **Bottom:** The image has been smoothed by a Gaussian function of $\sigma = 2.46''$.

TABLE 2
BEST FIT 2D MODEL PARAMETERS^a

Parameter	Circular Models ^b	Elliptical Models ^b	Units
qso.fwhm	0.43 ^{+0.02} _{-0.02}	0.26 ^{+0.02} _{-0.02}	arcsec
qso.xpos	4072.82 ^{+0.01} _{-0.01}	4072.82 ^{+0.01} _{-0.01}	physical
qso.ypos	3946.44 ^{+0.01} _{-0.01}	3946.43 ^{+0.01} _{-0.01}	physical
qso.ellip	–	0.115 ^{+0.097} _{-0.097}	
qso.theta	–	1.82 ^{+0.45} _{-0.45}	radians
qso.ampl	2018.5 ^{+165.8} _{-148.6}	1497.1 ^{+138.6} _{-138.6}	counts
clus.r0	3.03 ^{+0.25} _{-0.25}	3.58 ^{+0.31} _{-0.31}	arcsec
clus.xpos	4072.98 ^{+0.21} _{-0.21}	4072.96 ^{+0.21} _{-0.21}	
clus.ypos	3945.05 ^{+0.21} _{-0.21}	3945.06 ^{+0.22} _{-0.22}	
clus.ellip	–	0.300 ^{+0.015} _{-0.015}	
clus.theta	–	2.41 ^{+0.03} _{-0.03}	radians
clus.ampl	0.42 ^{+0.04} _{-0.04}	0.44 ^{+0.04} _{-0.04}	counts
clus.beta	0.48 ^{+0.17} _{-0.17}	0.48 ^{+0.17} _{-0.17}	
bgnd.c0	0.0023 ^{+0.0002} _{-0.0002}	0.0024 ^{+0.0001} _{-0.0001}	counts

^a Fit was performed on non-background subtracted image and the background model was included as a part of the model component: qso - 2D gaussian model; bgnd - 2D constant background model

clus - 2D beta model: $f(x, y) = f(r) = A(1 + (\frac{r}{r_0})^2)^{-3\beta+0.5}$;

$$r(x, y) = \sqrt{x'^2(1-\epsilon)^2 + y'^2(1+\epsilon)^2};$$

$x' = (x - x_o) \cos \theta + (y - y_o) \sin \theta$, $y' = (y - y_o) \cos \theta - (x - x_o) \sin \theta$ - the angle of ellipticity, ϵ - ellipticity.

^b 1σ uncertainties are shown for one interesting parameter.

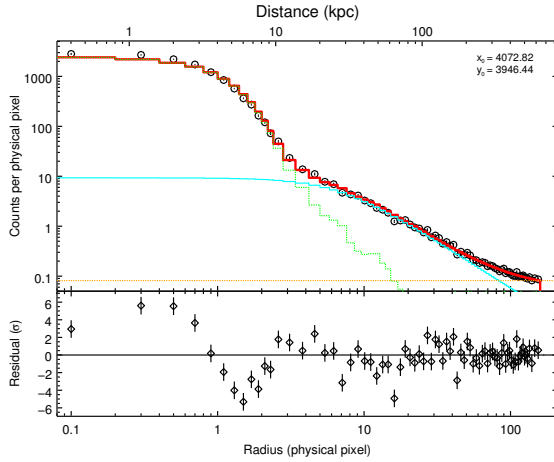


FIG. 2.— **Top panel:** Surface brightness profiles (in units of counts per pixel) centered on the quasar extracted from the data and the 2D circular models (see Table 2 for the best fit parameters). The location of the quasar centroid in physical coordinates is marked in the upper right corner. The surface brightness profile from the ACIS-S data is shown as black points with errorbars: data is binned to ensure at least 200 counts per bin. The model profiles are marked with solid lines: red - full model (qso + clus+ bgnd as defined in Table 2) convolved with ChART PSF; green - quasar (gauss2d only) model convolved with PSF (ie no cluster or background component). blue - cluster (beta2d), brown - background (cont2d). **Bottom panel:** Residuals between the full model and the data in units of σ . Physical pixel size is equal to $0.492''$, the size of the ACIS-S pixel.

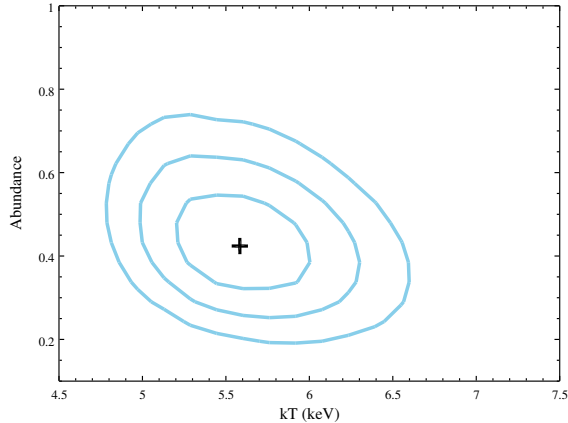


FIG. 3.— The confidence levels for the temperature and abundance parameters obtained in a global model fit to the cluster described in Sec. 3.2. The location of the best fit parameters is marked by a cross. Three levels 1σ , 2σ 3σ contours are shown.

We followed Russell et al. (2010), using the simulated *Chandra* PSF to understand the contribution from the central quasar to each individual annulus and the effects associated with a possible contamination of the cluster spectrum. We used CHART to simulate the quasar (point source) photons scattered by the *Chandra* mirrors, and MARX to project them onto the ACIS-S detector at the exact pointing as in the *Chandra* observations of 3C 186. In the CHART simulations we assumed the quasar photon flux to be described by the best model parameters fit to the spectrum extracted from a $r = 1.75''$ circular region centered on the quasar, i.e. an absorbed power law with N_H and $\Gamma = 1.9$. The simulated quasar image reflects both the scattering of the *Chandra* mirrors and an additional “blur” (parameter set to 0.3 in MARX) due to the standard dither and the aspect uncertainty. In Figure 5 we show a number of counts from the simulated quasar image in comparison to a number of counts detected by *Chandra* in each annulus assumed for the spectral modeling. The fraction of the total observed counts that can be associated with the quasar is shown in the bottom panel of the figure. It exceeds 10% only in the first innermost annulus.

In order to check the effects of quasar contamination on the spectral results, additional fits were performed wherein we included appropriately normalized power law model components to the cluster model for each annulus (see Table 4). The resulting temperatures and normalizations are in excellent agreement with the deprojected model results shown in Table 3. The only noticeable difference is for the innermost annulus, where the best fit temperature of $2.54^{+1.02}_{-0.57}$ is marginally lower (but still consistent within 1σ errors). We conclude that the quasar contribution does not significantly impact the deprojected fit parameters for the cluster observation.

Given the flux for the models in Table 3 and applying the appropriate K-correction, we find a total cluster luminosity $L_{0.5-2 \text{ keV}} = 4.6 \pm 0.2 \times 10^{44} \text{ erg s}^{-1}$.

3.3. Cluster Mass

We have measured gas mass and total mass profiles for the cluster using the Monte Carlo method of Allen et al. (2008). This analysis is also used to determine gas density and cooling time profiles for the cluster, which are shown in Figure 6. The density results are consistent with those obtained directly from the spectral fitting.

Our mass analysis uses a parameterized Navarro et al. (1995, 1997) (NFW) model, which is fitted directly to the observed cluster surface brightness profile and deprojected temperature profile (see Eq.1 and the description of the method in Allen et al. 2008). The best-fit NFW model has a concentration parameter $c = 7.4^{+2.8}_{-2.3}$, scale radius $r_s = 120^{+70}_{-40}$ kpc, and equivalent velocity dispersion $\sigma = 780^{+90}_{-60} \text{ km s}^{-1}$, with $\chi^2 = 7.9$ for five degrees of freedom. For these parameters we calculate the radius at which the mean enclosed mass density is 2500 times the critical density of the Universe at the redshift of the cluster, $r_{2500} = 283^{+18}_{-13}$ kpc. This results agrees well with the results of Allen et al. (2008) based on the earlier *Chandra* observation. However, the statistical uncertainties on r_{2500} are improved by a factor of ~ 4 .

The total mass within r_{2500} is $M_{2500} = 1.02^{+0.21}_{-0.14} \times 10^{14} M_\odot$. (Our 68 per cent error bars on M_{2500} also account for the uncertainty in r_{2500} .) The measured gas mass fraction with this radius, $f_{gas}(r_{2500}) = 0.129^{+0.015}_{-0.016}$, is consistent with the value determined by Allen et al. (2008) from the earlier, shorter observation, but with significantly reduced statistical uncertainties.

4. DISCUSSION

We have presented new, deep *Chandra* observations of the high redshift X-ray cluster associated with 3C 186, a luminous compact radio-loud quasar at $z = 1.067$ (Wills et al. 1992; Schneider et al. 2007). The new observations confirm the main results from our discovery paper (Siemiginowska et al. 2005), including the results on the global cluster temperature and central density profile. X-ray emission from the cluster is detected out to ~ 3 times larger distance from the quasar than was the case in the

TABLE 3
BEST FIT MODEL PARAMETERS

R ^a [arcsec]	Range [arcsec]	Total Counts ^b	Net Counts	kT [keV]	Norm ^c [1e-3]	CSTAT (dof=3550)	n _e [1e-2 cm ⁻³]
3.375	2.75-4.00	603.0±24.6	592.6±24.8	3.11 ^{+0.91} _{-0.64}	37.1149 ^{+6.0039} _{-5.6241}	2922.9	5.91 ^{+0.48} _{-0.45}
4.875	4.00- 5.75	773.0±27.8	751.8±28.2	5.97 ^{+1.64} _{-1.25}	13.4383 ^{+1.7655} _{-1.6035}	3064.0	3.62 ^{+0.22} _{-0.20}
6.5	5.75-7.25	538.0±23.2	513.9±23.7	4.81 ^{+1.61} _{-1.19}	7.4397 ^{+1.1952} _{-1.1136}	2976.1	2.65 ^{+0.21} _{-0.20}
8.75	7.25-10.25	892.0±29.9	827.1±30.9	7.11 ^{+2.43} _{-1.76}	2.6737 ^{+0.3014} _{-0.2533}	3231.4	1.59 ^{+0.09} _{-0.08}
12.75	10.25-15.25	1293.0±36.0	1135.2±38.1	7.77 ^{+2.93} _{-1.92}	1.0627 ^{+0.0996} _{-0.0857}	3388.9	1.00 ^{+0.05} _{-0.04}
18.25	15.25-21.25	1306.0±36.1	1034.8±39.7	6.95 ^{+2.88} _{-1.44}	0.4663 ^{+0.0422} _{-0.0371}	3460.2	0.66 ^{+0.03} _{-0.03}
25.625	21.25-30.00	1452.0±38.1	896.4±44.8	5.03 ^{+0.67} _{-0.65}	0.2781 ^{+0.0153} _{-0.0156}	3533.8	0.51 ^{+0.01} _{-0.01}

^a The assumed annuli are circular with the mean radius listed in the R column and ranges in Range column; ^b Total and net counts (in 0.5-7 keV range) summed within 4 observations in each region; ^c Normalization for APEC thermal model defined as $\text{Norm} = \frac{10^{-14}}{4\pi[D_A(1+z)]^2} \int n_e n_H dV$ with the abundance table set to Anders & Grevesse (1989); ^d listed uncertainties are at 68% for one interesting parameter.

TABLE 4
BEST FIT PARAMETERS FOR THE SIMULATED QUASAR DATA

R ^a [arcsec]	Γ	Norm ^b [1.e-7]
3.375	1.58 ^{+0.14} _{-0.13}	6.9 ^{+0.9} _{-0.8}
4.875	1.58 ^{+0.20} _{-0.17}	4.4 ^{+0.7} _{-0.7}
6.5	1.47 ^{+0.26} _{-0.24}	2.5 ^{+0.6} _{-0.5}
8.75	1.75 ^{+0.24} _{-0.23}	3.1 ^{+0.6} _{-0.5}
12.75	1.46 ^{+0.21} _{-0.18}	3.7 ^{+0.7} _{-0.6}
18.25	1.35 ^{+0.21} _{-0.18}	1.5 ^{+0.4} _{-0.4}
25.625	1.68 ^{+0.42} _{-0.35}	1.1 ^{+0.4} _{-0.4}

^a The assumed annuli are as in Table 3, e.g. circular with the centers listed in the R column; ^b Power law model normalization in photons cm⁻² s⁻¹ d listed uncertainties are at 68% for one interesting parameter.

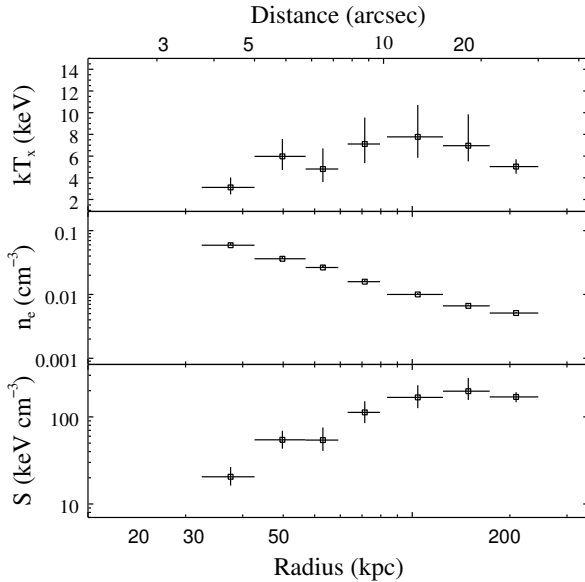


FIG. 4.— Deprojected temperature, density and entropy profiles for the best fit model parameters shown in Table 3.

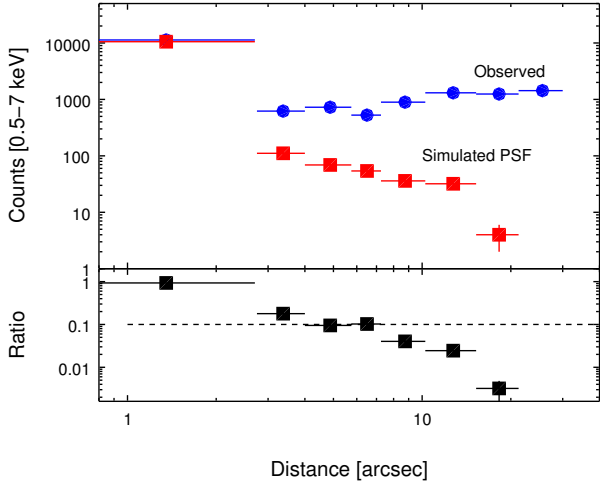


FIG. 5.— **Top panel:** A number of counts in the spectral extraction regions for the observed (quasar+cluster) emission (blue circles) and the CHART simulated PSF - red squares. The first data point shows the PSF normalized to the observed counts in the circular region with $r=2.7''$ centered on the quasar. **Lower panel:** The ratio of the simulated to the observed counts in each spectral region. The dashed line marks 0.1 value.

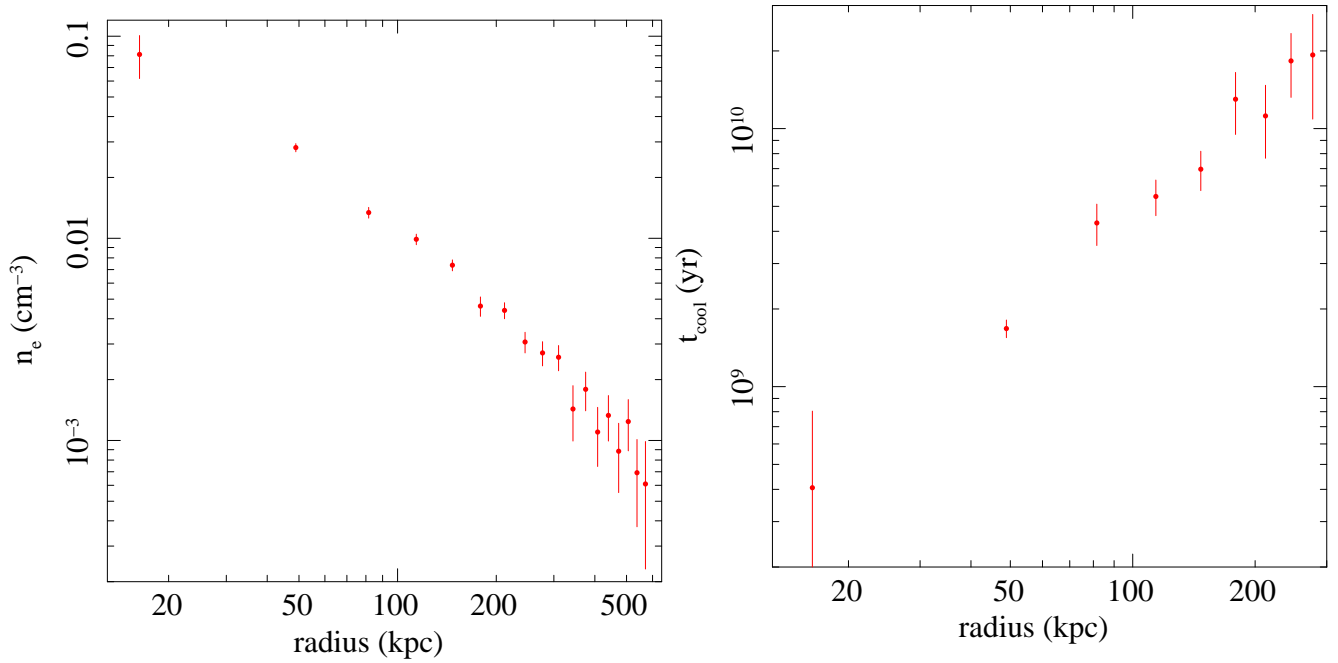


FIG. 6.— Density and cooling time profiles determined from the observed X-ray surface brightness and deprojected temperature profile, using the method of Allen et al. (2008). Error bars are 68% uncertainties. The results for the innermost bin include a conservative systematic allowance for uncertainties associated with modeling the central AGN emission.

first, short observation. The quasar is located within the center of the diffuse X-ray emission and only slightly offset (5.5 ± 0.9 kpc) from the centroid of the cluster's X-ray emission. The high signal to noise data and a larger cluster area uncovered in the new observations allowed for more detailed analysis of the properties of the cluster. Below we discuss the main results of these new X-ray observations.

4.1. Cooling core

The 3C186 X-ray cluster shows an elongated morphology that is detected out to $r > 500$ kpc. The cluster temperature profile has the characteristic shape of a cooling core cluster, with a sharp decline towards the center. The cluster is relatively cool in the outer ($r > 200$ kpc) regions with its temperature increasing slightly to a peak of $7.8_{-1.9}^{+2.4}$ keV at 100-200 kpc and then declining to $3.11_{-0.64}^{+0.91}$ keV in the central regions (Fig. 4). The electron density rises relatively smoothly from ~ 0.001 cm $^{-3}$ at $r \sim 500$ kpc to ~ 0.1 cm $^{-3}$, as one moves inward from $r=500$ kpc to the innermost resolved regions (Fig. 6). The sharp drop in entropy in the inner regions is also typical for cool core clusters.

The cooling time profile is shown in Figure 6. We measure cooling times at radii of 50 kpc and 25 kpc of $1.7 \pm 0.2 \times 10^9$ years and $7.5 \pm 2.6 \times 10^8$ years, respectively. We also measure nominal mass cooling rate (in the absence of cooling) of $400 \pm 190 M_{\odot} \text{year}^{-1}$ within the central 100 kpc. The cluster surrounding 3C 186 clearly possesses a very strong cooling core.

The measured core radius of $\sim 28.6 \pm 2.5$ kpc is small in comparison to typical core radii of nearby clusters. However, similarly small core radii have also been observed in other lower-redshift clusters with strongly cooling cores (e.g. Allen et al. 2001; Schmidt et al. 2001; Allen et al. 2002).

Observationally X-ray clusters divide into two classes: cool core clusters and non-cool core clusters. This division is based on the peak X-ray surface brightness and a central cooling time. Burns (1990) studied radio emission of central galaxies (cD) in a sample of Abell clusters and noticed that the cDs in cool core clusters were more likely than the ones in non-cool core clusters to be radio loud with a high radio power. More recent studies confirm that the cool core clusters are more likely to host a cD with both radio emission and H α emission lines (e.g. Sanderson et al. 2009; Haarsma et al. 2009). Mittal et al. (2009) reported that all strong cool core clusters harbor a central radio source, while 67% of the weak cool cores do, and 45% of the non-cool cores do.

3C186 cluster hosts a luminous quasar with broad lines and a compact radio structure fully contained within the host galaxy. 3C 186 is also a high redshift ($z = 1.06$) cluster with a strong cooling core. This is contradictory to the suggestion by Vikhlinin et al. (2007), based on a *Chandra* sample of X-ray clusters that there are no cool core clusters at $z > 0.5$. On the other hand more recent work (Santos et al. 2008; Alshino et al. 2010) indicates that the fraction of weak to moderate cool cores remains the same at high redshift and only the fraction of strong cool cores drops significantly.

Is 3C186 unique? It is interesting to note that a fraction of AGN in clusters increases with redshift (Martini et al.

2009), so high redshift clusters are more likely to host an AGN. An X-ray emission associated with AGN can confuse detection of a cooling core in a cluster at high redshift (Branchesi et al. 2007). Cool core clusters also have smaller cooling radii and their detection require high resolution X-ray observations. Therefore, samples of X-ray clusters used in studies of cool core evolution with redshift may be missing clusters associated with a strong AGN. We note that H1821+643 cluster at $z=0.3$ also has a strong cooling core that was observed by *Chandra* (Russell et al. 2010). Further studies of higher redshift clusters associated with AGN are needed in order to understand the evolution of cluster cooling with redshift.

4.2. Supermassive Black Hole Powering 3C186 Quasar

The black hole mass estimate for the 3C186 quasar from measurements of its broad emission lines is equal to $3 \times 10^9 M_{\odot}$ (Siemiginowska et al. 2005). The corresponding Eddington luminosity is equal to $L_{Edd} = 4 \times 10^{47}$ erg s $^{-1}$. The quasar optical-UV luminosity, based on the spectral energy distribution given in Siemiginowska et al. (2008a), is equal to $L_{UV} \sim 6 \times 10^{46}$ erg s $^{-1}$. Using a bolometric correction that ranges between $\sim 5 - 10$ (Elvis et al. 1994) we estimate the 3C186 bolometric luminosity to be of the order of $L_{bol} \sim 10^{47}$ erg s $^{-1}$ with the required accretion rate of $0.25 M_{Edd}$ critical rate.

The growth of this supermassive black hole might be closely related to the mass deposition from the cluster. If the cooling rate is $\sim 470 M_{\odot} \text{year}^{-1}$ then only a small fraction, $< 0.5\%$, of the cooling gas is needed to grow a $10^9 M_{\odot}$ black hole within the cooling time of the cluster's core. However, the mechanism of transporting this gas to the close vicinity of a central black hole is unclear.

4.3. Intermittent Radio Source

3C186 radio source belongs to a class of young CSS radio sources (see O'Dea 1998, for review). Murgia et al. (1999) measured a synchrotron age of $\sim 5 \times 10^5$ years for the entire radio structure. 3C186 has a double radio morphology with a one-sided jet. The double radio source has a total length equal to $1.8''$ (see Siemiginowska et al. (2005) and references therein) corresponding to 15 kpc projected size. A deprojected size is at least 30 kpc for < 30 degrees angle to our line of sight (based on the one-sided VLA jet), but probably not much larger (e.g., 100 kpc, or radius of 50 kpc, for ~ 9 degrees angle which is too small). Therefore we conclude that the 3C186 radio source is contained within the host galaxy.

Studies of compact radio sources suggest that they might have repetitive outbursts on short timescales of $\sim 10^3 - 10^5$ years (Baum et al. 1990; Reynolds & Begelman 1997; Owsianik et al. 1998; Czerny et al. 2009). In the case of the shortest timescales ($\sim 10^3$ years) the radio source does not have enough energy to grow beyond the host galaxy and it starts to recollapse within the host galaxy ISM. If there have been previous outbursts of the radio activity in 3C186 on the timescales longer than 3×10^4 years, the radio source would have been larger than the observed CSS structure. Our initial studies of the VLA radio data show a possible presence of an extended radio emission on scales of 10 arcsec (Siemiginowska et al. 2008a). However, this radio emission is seen at a very low significance

and more detailed analysis of new EVLA maps obtained recently have yet to confirm that this structure is real.

Most searches for X-ray clusters around radio-loud active galaxies have been focused on those with large-scale radio structures. Such radio structures are old, triggered a long time ago ($> 10^7$ years) and therefore have been interacting with the cluster environment for a long time. In nearby clusters, long term ($\sim 10^8$ years) intermittent radio activity of the central AGN is often imprinted into the X-ray morphology of the cluster in the form of bubbles, ripples or discontinuities in the surface brightness indicative of shocks (see McNamara & Nulsen 2007). GPS and CSS radio quasars are young ($< 10^5$ years Murgia et al. 1999; O’Dea 1998, for review) and have not developed large scale radio structures. These sources, if found in clusters, can potentially test the cluster heating process and the significance of the luminous quasar in the evolution of the cluster.

4.4. Quasars and X-ray Clusters

The majority of nearby clusters host a low power radio source with FRI radio morphology that have buoyantly rising bubbles filled with radio plasma. There are, however, a few examples of X-ray clusters associated with quasars or powerful radio galaxies at lower redshifts (for example Cygnus A, 3C 295 Allen et al. (2001), IRAS 09104+4109 Iwasawa et al. (2001), HS1821+643 Russell et al. (2010)). We note that the FRII radio source would have pressure driven radio lobes and jets and its X-ray morphology may be different than the one seen in clusters with FRI radio sources.

Cygnus A is a nearby FR II radio source embedded in a bright X-ray cluster (Carilli & Barthel 1996). The *Chandra* observations show a rich filamentary structure associated with the evolution of the radio source within the cluster and evidence for heating of the cluster gas (Wilson et al. 2000). However, the Cygnus A nucleus may not be in a luminous quasar phase although its radio power is high $L_R \sim 10^{45}$ erg s $^{-1}$ (Young et al. 2002; Steenbrugge et al. 2008). The nucleus is highly absorbed, i.e. $N_H \sim 2 \times 10^{23}$ cm $^{-2}$ as measured by Young et al. (2002), and correcting for the absorption gives the hard X-ray luminosity of 3.7×10^{44} erg s $^{-1}$. Young et al. (2002) estimated the optical luminosity to be consistent with Seyfert galaxies.

Another case of a relatively bright X-ray cluster detected around a lower redshift $z=0.322$ luminous quasar is HS1821+643 ($L_{bol} \sim 2 \times 10^{47}$ erg s $^{-1}$, Kolman et al. 1991; Crawford et al. 1999; Russell et al. 2010). This quasar has typical signatures of a quasar with broad lines and thermal emission in optical-UV band. It hosts a 300 kpc FRI radio source (Blundell & Rawlings 2001) that might be heating the cluster medium (Russell et al. 2010). The *Chandra* observation indicates complex interactions between the quasar and the cluster. However, the cluster properties are typical for the cool core cluster with a short central cooling time and the quasar does not appear to significantly impact the large scale cluster environment.

4.5. Cluster Heating

3C 186 is the first high redshift X-ray cluster known to host a luminous quasar and a compact radio source. The cluster X-ray morphology indicates that the cluster is well formed and has a cool core with a short central cooling time. The radio source can potentially supply the energy required to stabilize the cluster core against catastrophic cooling, as it expands into the cluster medium.

In Siemiginowska et al. (2005) we estimated the power of the radio jet using the Willott et al. (1999) (their Eq.12) relation between radio luminosity and jet power defined as $Q = 3 \times 10^{38} L_{151}^{6/7}$ W, where L_{151} is in units of 10^{28} W Hz $^{-1}$ sr $^{-1}$. Assuming the 3C 186 151 MHz flux density of 15.59 Jy (Hales et al. 1993) which accounts for the total radio source emission (the radio core is absorbed at this frequency) we find $L_{151} = 7.5 \times 10^{27}$ W Hz $^{-1}$ sr $^{-1}$ and then from the above equation we obtain the jet power of $L_{jet} = 2.4 \times 10^{45}$ erg s $^{-1}$. There is significant scatter in the Willott et al. (1999) relation, therefore this is an order of magnitude estimate.

The pressure in the radio lobes based on the radio flux density measurements and the equipartition assumption is $\sim 10^{-8}$ erg cm $^{-3}$ (Siemiginowska et al. 2005) and it exceeds the thermal pressure of the cluster $^4 \sim 4 \times 10^{-10}$ erg cm $^{-3}$ (for $kT = 3.1$ keV and $n = 0.08$ cm $^{-3}$). The overpressured radio source should drive a strong shock into the cluster medium and its expansion is not adiabatic. We can estimate a lower limit on the jet power from the equipartition measurements. Using the radio lobes volume of $\sim 10^{66}$ cm 3 (Siemiginowska et al. 2005) the minimum pressure gives a lower estimate of the instantaneous jet power, e.g. $\sim 10^{58}$ erg or $\sim 6 \times 10^{44}$ erg s $^{-1}$ for the age of the radio source of 5×10^5 years.

We note that the bolometric luminosity of 3C 186 is equal to $L_{bol} \sim 10^{47}$ erg s $^{-1}$ (see Sec.4.2) and the 3C 186 radiative power exceeds the jet kinetic power by at least a factor of 10. This is unusual for a cluster-center radio source and suggests that the so-called ‘quasar mode’ may be more important than the ‘radio mode’ for heating the 3C 186 cluster.

The process of transferring accretion energy into the cluster thermal energy is unclear. In the ‘radio mode’, the jet carries the energy from the black hole and deposits it into the cluster gas, e.g. via shocks. In the ‘quasar mode’, the radiation should be a dominant carrier of the accretion energy. King (2009) argues that for quasars with a black hole mass exceeding about $10^9 M_\odot$, radiation can be very efficient in initiating strong outflows that cause radiative shocks and result in cluster heating. On the other hand, quasar radiation energy can also be transferred directly to the cluster gas via Compton scattering.

We calculate the energy required to prevent significant cooling of the cluster core in 3C 186 following King (2009). The mass of the gas within the cooling radius of 45 kpc assuming the central density of 0.08 cm $^{-3}$ is equal to $M_{core} = 3.3 \times 10^{11} M_\odot$. The amount of energy required to heat this gas is of the order of 1 keV per baryon, e.g. $E_{heat} \sim (1\text{keV}/1\text{GeV}) M_{core} c^2 \sim 10^{-6} M_{core} c^2 \sim 6 \times 10^{59}$ erg. The observed quasar luminosity of $\sim 10^{47}$ erg s $^{-1}$ provides enough energy to heat the cluster core within about 2×10^5 years if the heating process were 100 percent efficient. However, the cooling time of the core is much

⁴ Note Siemiginowska et al. (2005) gives a factor of 10 lower value which is a mistake.

longer, $\sim 7 \times 10^8$ years, and only a very small fraction of the observed luminosity is needed to support the cluster heating within that time.

We estimate the efficiency of transferring the radiation energy into the cluster. The opacity of the cluster gas in the core to Compton scattering is equal to $\tau = n_e r_0 \sigma_T \sim 0.008$, assuming the average particle density of $n_e = 0.075 \text{ cm}^{-3}$, $r_0 = 45 \text{ kpc}$ core radius, and σ_T is the Thomson cross section. This means that about 0.8% of the quasar photons will interact with cluster gas and may heat up the cluster. We note also that only the photons with energies higher than $\sim 1 \text{ keV}$ will be able to heat⁵ the cluster gas to the required temperatures which reduces the amount of available photons by a factor of 10. We also assumed spherical symmetry and if we include a covering factor of 30% that accounts for cold gas in the central regions (e.g. torus), the total number of photons decreases to about 0.3%. This results in the available instantaneous power of $0.003 \times 10^{46} \text{ erg s}^{-1}$ which is equivalent to a total energy of $\sim 7 \times 10^{59} \text{ erg}$ available to balance the cluster cooling within 7×10^8 years. This is within an order of magnitude of the required energy to balance the cluster cooling. However, this also requires that the quasar is powered by accreting at $0.25 \dot{M}_{Edd}$ rate, (e.g. $\sim 18 \dot{M}_{\odot} \text{ year}^{-1}$ assuming standard 10% accretion efficiency), continuously during the cooling time of the cluster, which results in the final required amount of fuel exceeding by a factor of 4 the current black hole mass. Although such an amount of fuel is only a fraction of the available mass in the cluster core, it is unclear how it can be funneled down to the center within close vicinity of a black hole.

King (2009) suggested that the radiation pressure in the luminous quasars will generate a wind, so the radiation energy is transferred to the kinetic energy of the wind and then to the cluster gas via radiative shocks. This mechanism also requires a large amount of fuel supply.

We should comment here that the young CSS radio sources, such as 3C186, might be intermittent on short timescales $\sim 10^5$ years if the accretion rates are close to the Eddington value. (Czerny et al. 2009). The source experiences transitions between (1) a high super-Eddington state characterize by a luminous accretion disk and a powerful jet; and (2) a quiescent state with the sub-Eddington luminosity of the disk and no jet. In this scenario the super-Eddington state should last longer than $\sim 10^3$ years for a radio source to grow beyond the host galaxy, as the expansion of the radio source within the host galaxy takes more than $\sim 10^6$ years. During that initial time the luminous quasar can provide enough radiative power to heat up a small cluster core. At later times when the radio source grows beyond the host galaxy and expands within the cluster environment the mechanical energy is directly used to prevent cluster cooling.

4.6. Clusters at High Redshift and Cosmology

X-ray observations of galaxy clusters at high redshift can provide strong constraints on cosmological parameters (see Vikhlinin (2010) for a recent review). In hierarchical models of cluster formation, the high-mass end of the

mass function is the most sensitive to the linear growth of the fluctuations (Linder & Jenkins 2003). Thus the evolution of the number density of massive clusters that traces the growth of the density fluctuation can be used to constrain the dark energy equation of state parameter w (Haiman et al. 2001; Vikhlinin et al. 2009; Mantz et al. 2009). The gas mass fraction of clusters can also be used to test the cosmological parameters (Allen et al. 2008, 2004) and provide independent constraints on w .

Allen et al. (2008) measured $f_{gas}(r_{2500})$ for 42 clusters at $0 < z < 1.1$ and obtained an average value of $f_{gas}(r_{2500}) = 0.1104 \pm 0.0003$. Their study included the previous, short observation of the 3C186 cluster (15ks good time), which was the highest redshift cluster in their sample. The measured gas mass fraction for this target by Allen et al. (2008) was $f_{gas}(r_{2500}) = 0.1340 \pm 0.0777$. Our new measurement of $f_{gas}(r_{2500}) = 0.129_{-0.016}^{+0.015}$ is consistent with the previous value, but improves the statistical uncertainties by a factor of $\sim 4 - 5$. Our new f_{gas} measurement for the 3C186 cluster is also consistent, within measurement errors, with the mean value determined at lower redshifts, arguing against any strong evolution of the $f_{gas}(r_{2500})$ value for massive, relaxed clusters over the redshift range $0 < z < 1.1$.

A relatively small number of X-ray clusters at $z > 1$ have been observed so far (The BAX⁶ (Sadat et al. 2004) data base lists 17 $z > 1$ clusters to date). New methods to search for high-redshift X-ray clusters are providing new discoveries of massive clusters, including the recent discovery of the most distant X-ray cluster at $z = 1.99$ (Andreon et al. 2009). The 3C186 cluster is so far the only spectroscopically confirmed cooling core cluster at such high redshifts, and the only one known to host a luminous quasar at the center. The cluster global temperature, $kT = 5.74 \text{ keV}$ is not extreme when compared to the other massive clusters at $z > 1$, although the X-ray luminosity, $L_{0.5-2\text{keV}} = 6.4 \times 10^{44} \text{ erg s}^{-1}$, exceeds that of the next most luminous cluster detected so far, *XMMU J2235.3-2557* (Rosati et al. 2009) at $z = 1.39$. The measured 3C186 cluster metallicity lies slightly above the mean trend with redshift discussed by Balestra et al. (2007). More detailed evolutionary studies should soon become possible with improved high redshift cluster samples from *Chandra* and *XMM-Newton*.

5. SUMMARY AND CONCLUSIONS

We have presented results from a deep (200ks) *Chandra* image of the hot ($kT = 5.6 \pm 0.3 \text{ keV}$), X-ray luminous galaxy cluster surrounding the powerful quasar 3C186 at a redshift $z = 1.067$. The spatially resolved temperature profile, entropy, density and cooling time profiles all confirm 3C186 as a cooling core cluster. The measured gas mass fraction of $f_{gas} = 0.129_{-0.016}^{+0.015}$ at r_{2500} is consistent with measurements for lower redshift systems. This argues against strong evolution in $f_{gas}(z)$ at r_{2500} for massive, relaxed systems. Cooling gas in the cluster core can in principle support the growth of a supermassive black hole and power the luminous quasar. The radiative power of the quasar exceeds the kinematic power, suggesting that ra-

⁵ We note that the UV photons will also cool the cluster gas, however the total energy contained in the quasar spectrum above $> 1 \text{ keV}$ exceeds the energy in the UV band. The heating-cooling balance of the cluster gas has to be modeled properly to understand the heating efficiency.

⁶ <http://bax.ast.obs-mip.fr/>

diative heating may be important at intermittent intervals in cluster cores.

ACKNOWLEDGMENTS

We thank the anonymous referee for comments that greatly improved the manuscript. AS thanks Mitch Begelman and Anna Wolter for comments. We thank Agnieszka

Siemiginowska for English improvement to the text. This research is funded in part by NASA contract NAS8-39073. Partial support for this work was provided by the *Chandra* grants GO2-3148A, GO5-6113X and GO8-9125A-R. Basic research in radio astronomy at the NRL is supported by 6.1 Base funding.

REFERENCES

- Allen, S. W., Rapetti, D. A., Schmidt, R. W., Ebeling, H., Morris, R. G., & Fabian, A. C. 2008, *MNRAS*, 383, 879
- Allen, S. W., Schmidt, R. W., Ebeling, H., Fabian, A. C., & van Speybroeck, L. 2004, *MNRAS*, 353, 457
- Allen, S. W., Schmidt, R. W., & Fabian, A. C. 2002, *MNRAS*, 335, 256
- Allen, S. W., et al. 2001, *MNRAS*, 324, 842
- Alshino, A., Ponman, T., Pacaud, F., & Pierre, M. 2010, arXiv:1005.4958
- Anders E. & Grevesse N. 1989, *Geochimica et Cosmochimica Acta* 53, 197
- Andreon, S., Maughan, B., Trinchieri, G., & Kurk, J. 2009, *A&A*, 507, 147
- Begelman, M. C., & Cioffi, D. F. 1989, *ApJ*, 345, L21
- Balestra, I., Tozzi, P., Ettori, S., Rosati, P., Borgani, S., Mainieri, V., Norman, C., & Viola, M. 2007, *A&A*, 462, 429
- Ball, R., Burns, J. O., & Loken, C. 1993, *AJ*, 105, 53
- Baum, S. A., O’Dea, C. P., Murphy, D. W., & de Bruyn, A. G. 1990, *A&A*, 232, 19
- Begelman, M. C., King, A. R., & Pringle, J. E. 2006, *MNRAS*, 370, 399
- Belsole, E., Worrall, D. M., Hardcastle, M. J., & Croston, J. H. 2007, *MNRAS*, 381, 1109
- Best, P. N., von der Linden, A., Kauffmann, G., Heckman, T. M., & Kaiser, C. R. 2007, *MNRAS*, 379, 894
- Birzan, L., McNamara, B. R., Nulsen, P. E. J., Carilli, C. L., & Wise, M. W. 2008, *ApJ*, 686, 859
- Branchesi, M., Gioia, I. M., Fanti, C., & Fanti, R. 2007, *A&A*, 472, 727
- Blundell, K. M., & Rawlings, S. 2001, *ApJ*, 562, L5
- Burke, D. et al 2009, in preparation
- Burns, J. O. 1990, *AJ*, 99, 14
- Carilli, C. L., & Barthel, P. D. 1996, *A&ARv*, 7, 1
- Cash, W. 1979, *ApJ*228, 939
- Celotti, A., & Fabian, A. C. 2004, *MNRAS*, 353, 523
- Crawford, C. S. & Fabian, A.C. 1993, *MNRAS*, 260, L15
- Crawford, C. S., & Fabian, A. C. 2003, *MNRAS*, 339, 1163
- Crawford, C. S., Lehmann, I., Fabian, A. C., Bremer, M. N., & Hasinger, G. 1999, *MNRAS*, 308, 1159
- Croston, J. H., Hardcastle, M. J., Harris, D. E., Belsole, E., Birkinshaw, M., & Worrall, D. M. 2005, *ApJ*, 626, 733
- Czerny, B., Siemiginowska, A., Janiuk, A., Nikiel-Wroczyński, B., & Stawarz, L. 2009, *ApJ*, 698, 840
- Ellingson, E., Yee, H. K. C., & Green, R. F. 1991, *ApJ*, 371, 49
- Ellingson, E., Green, R. F., & Yee, H. K. C. 1991, *ApJ*, 378, 476
- Elvis, M., et al. 1994, *ApJS*, 95, 1
- Ettori, S., Tozzi, P., Borgani, S., & Rosati, P. 2004, *A&A*, 417, 13
- Fabian, A. C., Hu, E. M., Cowie, L. L., & Grindlay, J. 1981, *ApJ*, 248, 47
- Fabian, A. C. 1994, *ARA&A*, 32, 277
- Fabian, A. C., Sanders, J. S., Crawford, C. S., & Ettori, S. 2003, *MNRAS*, 341, 729
- Freeman, P., Doe, S., & Siemiginowska, A. 2001, *Proc. SPIE*, 4477, 76
- Giozzi, M., Brinkmann, W., Laurent-Muehleisen, S. A., Takalo, L. O., & Sillanpää, A. 1999, *A&A*, 352, 437
- Haiman, Z., Mohr, J. J., & Holder, G. P. 2001, *ApJ*, 553, 545
- Hales, S. E. G., Baldwin, J. E., & Warner, P. J. 1993, *MNRAS*, 263, 25
- Hall, P. B., Ellingson, E., Green, R. F., & Yee, H. K. C. 1995, *AJ*, 110, 513
- Hall, P. B., Ellingson, E., & Green, R. F. 1997, *AJ*, 113, 1179
- Hardcastle, M. J., & Worrall, D. M. 1999, *MNRAS*, 309, 969
- Harris, D. E., & Krawczynski, H. 2006, *ARA&A*, 44, 463
- Haarsma, D. B., et al. 2009, arXiv:0911.2798
- Hicks, A. K., et al. 2008, *ApJ*, 680, 1022
- Iwasawa, K., Fabian, A. C., & Ettori, S. 2001, *MNRAS*, 321, L15
- Kauffmann, G., Heckman, T. M., & Best, P. N. 2008, *MNRAS*, 384, 953
- Kataoka, J., & Stawarz, L. 2005, *ApJ*, 622, 797
- King, A. 2009, *ApJ*, 695, L107
- Kolman, M., Halpern, J. P., Shrader, C. R., & Filippenko, A. V. 1991, *ApJ*, 373, 57
- Kriss, G. A., Cioffi, D. F., & Canizares, C. R. 1983, *ApJ*, 272, 439
- Linder, E. V., & Jenkins, A. 2003, *MNRAS*, 346, 573
- Mantz, A., Allen, S. W., Rapetti, D., & Ebeling, H. 2009, arXiv:0909.3098
- Martini, P., Sivakoff, G. R., & Mulchaey, J. S. 2009, *ApJ*, 701, 66
- McNamara et al. 2005, *Nature* 433, 45.
- McNamara, B. R., & Nulsen, P. E. J. 2007, *ARA&A*, 45, 117
- Mittal, R., Hudson, D. S., Reiprich, T. H., & Clarke, T. 2009, *A&A*, 501, 835
- Murgia, M., Fanti, C., Fanti, R., Gregorini, L., Klein, U., Mack, K.-H., & Vigotti, M. 1999, *A&A*, 345, 769
- Navarro, J. F., Frenk, C. S., & White, S. D. M. 1997, *ApJ*, 490, 493
- Navarro, J. F., Frenk, C. S., & White, S. D. M. 1995, *MNRAS*, 275, 720
- Nelder, J.A. & Mead, R. 1965, *Computer Journal*, vol7, pp.308-313
- Nipoti, C., & Binney, J. 2005, *MNRAS*, 361, 428
- O’Dea, C. P. 1998, *PASP*, 110, 493
- Owsianik, I., Conway, J. E., & Polatidis, A. G. 1998, *A&A*, 336, L37
- Rafferty, D. A., McNamara, B. R., Nulsen, P. E. J., & Wise, M. W. 2006, *ApJ*, 652, 216
- Refsdal, B.L., et al. in Proceedings of the 8th Python in Science Conference, held in Pasadena in Aug.2009, Edt. Varaquaux, van der Walt and Millman, p. 51-57
- Reynolds, C. S., & Begelman, M. C. 1997, *ApJ*, 487, L135
- Rosati, P., et al. 2009, *A&A*, 508, 583
- Russell, H. R., Fabian, A. C., Sanders, J. S., Johnstone, R. M., Blundell, K. M., Brandt, W. N., & Crawford, C. S. 2010, *MNRAS*, 402, 1561
- Ruszkowski & Springel, 2009, *ApJ*, 696, 1094
- Sadat, R., Blanchard, A., Kneib, J.-P., Mathez, G., Madore, B., & Mazzarella, J. M. 2004, *A&A*, 424, 1097
- Sanderson, A. J. R., O’Sullivan, E., & Ponman, T. J. 2009a, *MNRAS*, 395, 764
- Sanderson, A. J. R., Edge, A. C., & Smith, G. P. 2009, *MNRAS*, 398, 1698
- Santos, J. S., et al. 2009, *A&A*, 501, 49
- Santos, J. S., Rosati, P., Tozzi, P., B’Ohringer, H., Ettori, S., & Bignamini, A. 2008, *Astronomical Society of the Pacific Conference Series*, 399, 375
- Sarazin, C. L., Koekemoer, A. M., Baum, S. A., O’Dea, C. P., Owen, F. N., & Wise, M. W. 1999, *ApJ*, 510, 90
- Schmidt, R. W., Allen, S. W., & Fabian, A. C. 2001, *MNRAS*, 327, 1057
- Schneider, D. P., et al. 2007, *AJ*, 134, 102
- Shen, S., Kauffmann, G., von der Linden, A., White, S. D. M., & Best, P. N. 2008, *MNRAS*, 389, 1074
- Siemiginowska, A., Cheung, C. C., LaMassa, S., Burke, D. J., Aldcroft, T. L., Bechtold, J., Elvis, M., & Worrall, D. M. 2005, *ApJ*, 632, 110
- Siemiginowska, A., LaMassa, S., Aldcroft, T. L., Bechtold, J., & Elvis, M. 2008, *ApJ*, 684, 811
- Siemiginowska, A., Aldcroft, T. L., Burke, D., Bechtold, J., Cheung, C. C., Lamassa, S., & Worrall, D. M. 2008, *Extragalactic Jets: Theory and Observation from Radio to Gamma Ray*, 386, 350
- Smith, E. P., & Heckman, T. M. 1990, *ApJ*, 348, 38
- Spergel, D. N., et al. 2003, *ApJS*, 148, 175
- Steenbrugge, K. C., Blundell, K. M., & Duffy, P. 2008, *MNRAS*, 388, 1465
- Sun, M., Voit, G. M., Donahue, M., Jones, C., Forman, W., & Vikhlinin, A. 2009, *ApJ*, 693, 1142
- Vikhlinin, A., VanSpeybroeck, L., Markevitch, M., Forman, W. R., & Grego, L. 2002, *ApJ*, 578, L107
- Vikhlinin, A., Kravtsov, A., Forman, W., Jones, C., Markevitch, M., Murray, S. S., & Van Speybroeck, L. 2006, *ApJ*, 640, 691
- Vikhlinin, A., Burenin, R., Forman, W. R., Jones, C., Hornstrup, A., Murray, S. S., & Quintana, H. 2007, *Heating versus Cooling in Galaxies and Clusters of Galaxies*, 48
- Vikhlinin, A., et al. 2009, *ApJ*, 692, 1060
- Vikhlinin, A. 2010, *Proceedings of the National Academy of Science*, 107, 7179

- Wills, B. J., Wills, D., Breger, M., Antonucci, R. R. J., & Barvainis, R. 1992, *ApJ*, 398, 454
- Willott, C. J., Rawlings, S., Blundell, K. M., & Lacy, M. 1999, *MNRAS*, 309, 1017
- Weisskopf, M. C., Tananbaum, H. D., Van Speybroeck, L. P., & O'Dell, S. L. 2000, *Proc. SPIE*, 4012, 2
- Wilson, A. S., Young, A. J., & Shopbell, P. L. 2000, *ApJ*, 544, L27
- Worrall, D.M., Lawrence, C.R., Pearson, T.J. & Readhead, A.C.S. 1994, *ApJ*, 420, L17
- Worrall, D.M., Birkinshaw, M. & Hardcastle, M.J. 2000, in *Large Scale Structure in the X-ray Universe*, ed. M. Plionis & I. Georganopoulos, Atlantisciences 2000, ISBN 2-84394-227-6, 195–198
- Worrall, D. M., Hardcastle, M. J., Pearson, T. J., & Readhead, A. C. S. 2004, *MNRAS*, 347, 632
- Worrall, D. M., & Birkinshaw, M. 2006, in “Physics of Active Galactic Nuclei at all Scales”, *Lecture Notes in Physics*, 693, 39
- Yee, H. K. C., & Ellingson, E. 1993, *ApJ*, 411, 43
- Young, A. J., Wilson, A. S., Terashima, Y., Arnaud, K. A., & Smith, D. A. 2002, *ApJ*, 564, 176

APPENDIX

A1: Modeling Background Spectra

We used *Sherpa* to fit simultaneously source and background data in the spectral analysis of the cluster. A “blank-sky” background file `acis7sD2005-09-01bkgrnd_ctiN0001.fits` provided by the *Chandra* X-ray Center was used to define a background model. First we filtered and reprojected X-ray events contained in this background file following the CIAO Thread *The ACIS "Blank-Sky" Background Files*⁷. Next we extracted a spectrum from a box region (`rotbox(4385.5,4112.5,980,990,0)`, the first two values show a center of the box, the next ones the size of the box in ACIS pixels, and a rotation angle) and corresponding instrument response files using `specextract` tool in CIAO. We fit this spectrum in *Sherpa* using a combination of an 8th-order polynomial and 9 gaussian lines getting the best-fit model with the statistics equal to `cstat=540.8` (443 d.o.f). Figure 7 shows the resulting fit and residuals.

We next checked how well this empirical model fits the background data in the observations. We applied the background model to the background spectra in each obsid and fit only the model normalization. The resulting fit statistics is equal to `cstat=1900.4` (1772 d.o.f.) for the simultaneous background fit to all four observations. Figure 8 shows the fit result for the obsid 9408 with the highest background counts in the spectrum.

In the final simultaneous source and background fitting of the cluster spectra the background normalization was varied and appropriate background model predicted counts were included in the total model predicted counts. An additional constant scaling accounts for a difference in exposure times and areas of the background and source regions and it is automatically applied by *Sherpa* during the fit.

⁷ <http://cxc.harvard.edu/ciao/threads/acisbackground/index.py.html>

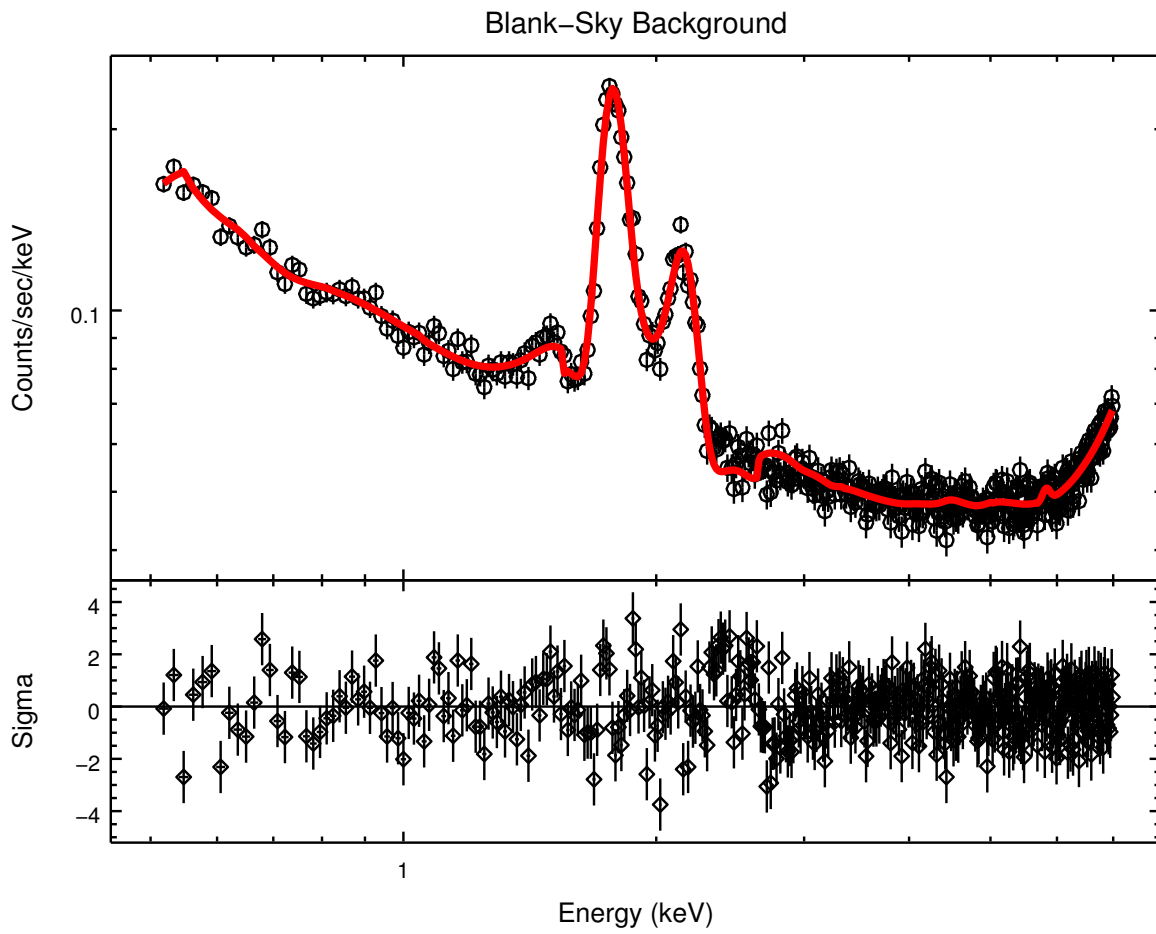


FIG. 7.— **Top panel:** Blank-sky background data fit with the complex model: polynomial + 9 gauss lines. **Lower panel:** Residuals.

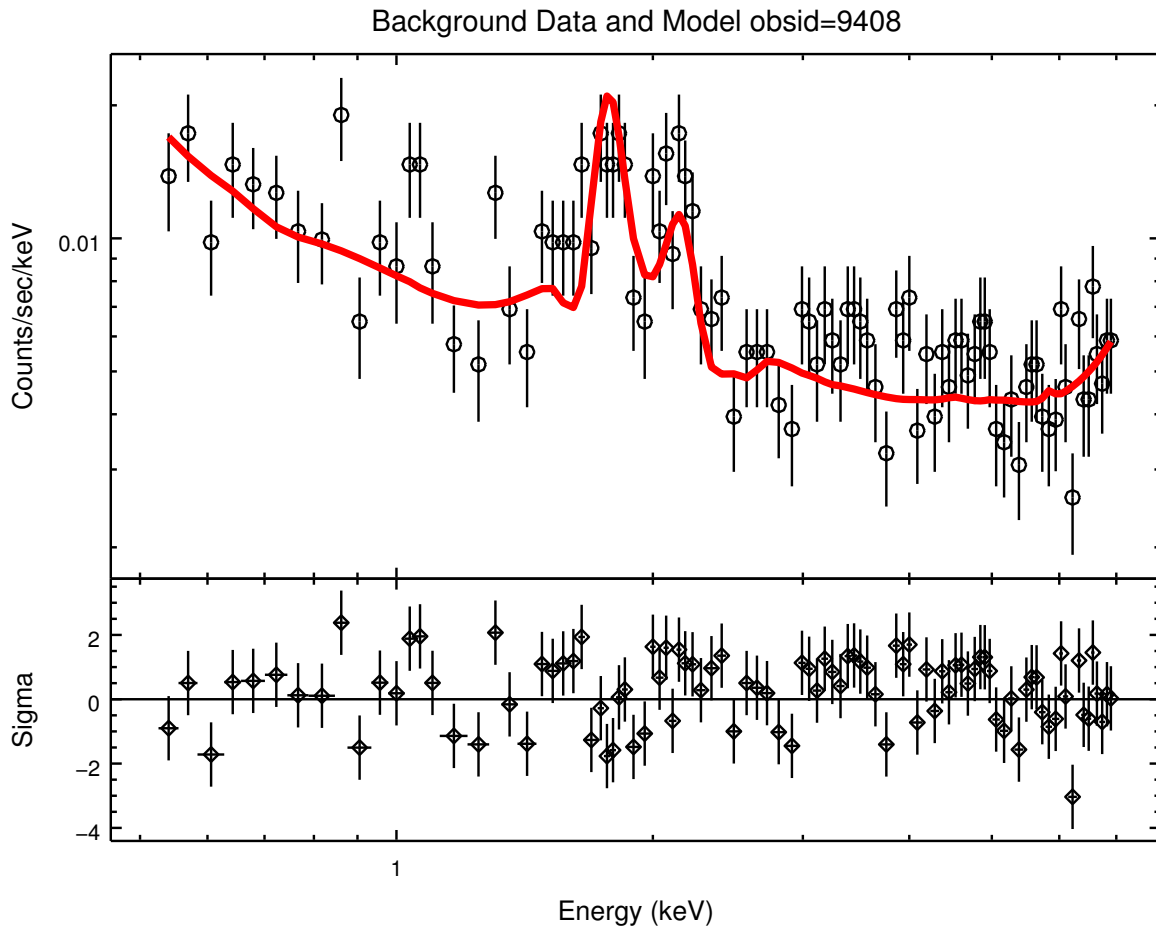


FIG. 8.— The background spectrum for obsid 9408 fit with the same shape background model as the blank-sky data shown in Fig. 7. Top panel shows the data marked with points and a model drawn with a red solid line. The bottom panel shows the residuals. The data were grouped by 15 counts per bin for the visualization only.